UltraBones100k: An Ultrasound Image Dataset with CT-Derived Labels for Lower Extremity Long Bone Surface Segmentation

Luohong Wu^{1*}, Nicola A. Cavalcanti¹, Matthias Seibold¹, Giuseppe Loggia², Lisa Reissner², Jonas Hein^{1,3}, Silvan Beeler², Arnd Viehöfer², Stephan Wirth², Lilian Calvet¹, Philipp Fürnstahl¹

¹Research in Orthopedic Computer Science, University Hospital Balgrist, University of Zurich, Switzerland. ²Department of Orthopedic Surgery, University Hospital Balgrist, University of Zurich, Switzerland. ³Computer Vision Geometry, ETH Zurich, Switzerland.

*Corresponding author(s). E-mail(s): luohong.wu@balgrist.ch;

Abstract

Purpose: Ultrasound-based bone surface segmentation is crucial in computer-assisted orthopedic surgery. However, ultrasound images have limitations, including a low signal-to-noise ratio, acoustic shadowing, and speckle noise, which make interpretation difficult. Existing deep learning models for bone segmentation rely primarily on costly manual labeling by experts, limiting dataset size and model generalizability. Additionally, the complexity of ultrasound physics and acoustic shadow makes the images difficult for humans to interpret, leading to incomplete labels in low-intensity and anechoic regions and limiting model performance. To advance the state of the art in ultrasound bone segmentation and establish effective model benchmarks, larger and higher-quality datasets are needed.

Methods: We propose a methodology for collecting ex-vivo ultrasound datasets with automatically generated bone labels, including anechoic regions. The proposed labels are derived by accurately superimposing tracked bone Computed Tomography (CT) models onto the tracked ultrasound images. These initial labels are refined to account for ultrasound physics. A clinical evaluation is conducted by an expert physician specialized on orthopedic sonography to assess the quality of the generated bone labels. A neural network for bone segmentation is trained

on the collected dataset and its predictions are compared to expert manual labels, evaluating accuracy, completeness, and F1-score.

Results: We collected the largest known dataset of 100k ultrasound images of human lower limbs with bone labels, called UltraBones100k. A Wilcoxon signed-rank test with Bonferroni correction confirmed that the bone alignment after our optimization pipeline significantly improved the quality of bone labeling (p < 0.001). The model trained on UltraBones100k consistently outperforms manual labeling in all metrics, particularly in low-intensity regions (320% improvement in completeness at a distance threshold of 0.5 mm).

Conclusion: This work is promising to facilitate research and clinical translation of ultrasound imaging in computer-assisted interventions.

Keywords: Bone segmentation, Bone surface segmentation, Bone annotation, Ultrasound image analysis, Computer-assisted orthopedic surgery

1 Introduction

Ultrasound is a well-established imaging technology widely used in the clinical diagnosis of musculoskeletal pathologies, including bone and soft tissue injuries [1]. It also facilitates dynamic assessments of joint and tendon movements, stability[2], and the detection of fracture healing, structural abnormalities, infections, ligament injuries, nerve compression, and mechanical impingement [3]. As evidenced by a substantial body of literature [4–8], the segmentation and 3D reconstruction of ultrasound are gaining increasing significance as a powerful modality in interventional Computer-Assisted Orthopedic Surgery (CAOS) systems. Compared to ionizing imaging modalities like fluoroscopy, ultrasound offers advantages in improving guidance and navigation during interventional and surgical procedures[4], including trauma treatment[6], needle placement, and robotic surgery [5].

Accurate 3D modeling of bone geometry requires precise identification and segmentation of bone anatomies, which relies heavily on high-quality labels produced by expert professionals. Due to the highest acoustic impedance compared to surrounding soft tissues, bones typically appear as high-intensity regions when the ultrasound probe is perpendicular to the bone surface. This phenomenon holds true across various bones and individuals, facilitating robust computer-based segmentation of bones in ultrasound images. However, when the probe is positioned at a larger oblique angle to the bone surface, bones can appear as low-intensity regions as most portion of acoustic energy is reflected into surrounding soft tissues instead of back to the probe. These low-intensity regions can only be inferred by surgeons through anatomical knowledge but cannot be accurately labeled. The same applies to fully anechoic regions formed by the complete absorption of the ultrasound signal in the overlying bone layers.

To address these challenges, various medical imaging methods based on handcrafted features have been developed to enhance the interpretation of ultrasound images [9, 10]. Recently, deep learning-based bone segmentation methods have shown promising improvements in robustness, accuracy, and processing speed [7, 8, 11–13]. However, the performance of such models relies on the quality of the labeled training dataset, which cannot be produced on a large scale if relying solely on human experts. The resulting datasets are often small (ranging from dozens to thousands labeled slices), limiting the performance and generalization of the trained models. Additionally, most existing methods train and validate their models on non-public datasets and use non-standardized evaluation metrics, making it difficult to compare and benchmark the performance of different models across studies [14, 15]. The absence of large-scale, accurately labeled public datasets has been a critical obstacle for the community in developing more advanced models.

In this work, we propose a methodology for collecting ultrasound datasets with automatically generated bone labels. Instead of relying on manual labeling, our approach utilizes tracked CT bone model to tackle the problem of identifying obscured, low-intensity bone regions, resulting in more precise and complete labels. With this methodology, we have collected a dataset of 100k annotated ultrasound images with bone labels from 14 human cadaveric lower legs, called UltraBones100k. We hypothesize that the information in UltraBones100k is sufficient for deep learning models to segment both high intensity and low intensity bone regions. A deep learning model for bone segmentation is trained on UltraBones100k, which significantly outperforms manual segmentation performed by an expert surgeon.

The dataset, as well as the trained model, is available for download here¹.

2 Related Work

Ultrasound Bone Segmentation. Numerous intensity-based bone segmentation methods have been developed [14, 15]. However, intensity-based methods face challenges in terms of robustness and accuracy. To mitigate these issues, frequency-based methods have been introduced, including phase symmetry and structured phase symmetry techniques [9, 10], which aim to enhance bone boundaries. With the advent of deep learning, neural network models such as CNNs, U-nets, and GANs have been employed for bone segmentation in ultrasound images, targeting various anatomical regions such as the spine [7, 11], pelvis [8], femur [8, 12, 13], tibia [8, 12, 13], fibula [12], and radius [12, 13]. These deep learning methods have demonstrated superior performance over traditional approaches in terms of accuracy, robustness, and runtime. For example, average bone surface distance errors have been reported to range from 0.2 mm to 1.7 mm [7, 13, 16]. Based on accurate 2D bone segmentation results, the reconstructed bone surfaces achieve sub-millimetric one-sided CD [17]. However, these studies rely on small non-public datasets with manually labeled bone structures and fail to use effective separate validation and test sets, limiting the generalizability of trained models. The absence of standardized evaluation metrics, with over 18 different metrics in use [14], further hinders effective model benchmarking and comparison.

Automatic labeling. Optical tracking markers have been applied in the medical imaging community for collecting datasets with automatically generated labels, such as tracked spine CT models [18] and surgical instruments [19]. So far, one previous work has attempted to automatically generate bone labels in ultrasound images using

 $^{^{1}\}mathrm{Link}$ will be available upon acceptance.

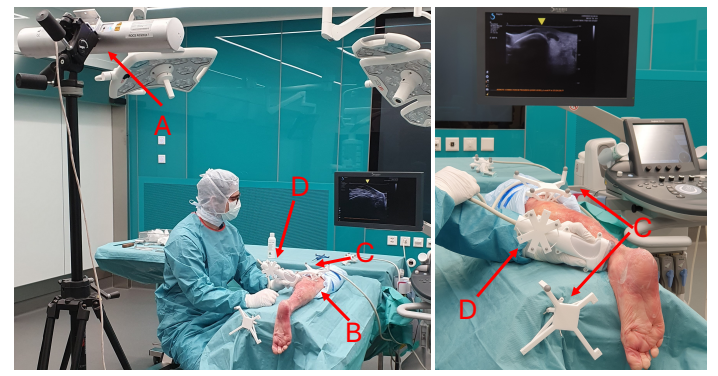


Fig. 1: The dataset acquisition setup includes an optical tracking system (A), a human cadaveric specimen (B) with mounted optical markers (C), and an tracked and calibrated ultrasound device (D).

a tracked bone CT model [20]. However, their approach led to significant alignment errors due to error accumulation, ultimately requiring a fallback to manual labeling. Image-based multi-modal registration methods, such as CT-US registration in Imfusion Suite ², can also be used to automatically align CT-US data. However, as we will demonstrate, these methods do not provide sufficient accuracy for automatic labeling.

3 Method

3.1 Dataset Collection and Automatic Bone labeling

Acquisition Setup. Our dataset acquisition setup using human cadaveric specimens is illustrated in Figure 1.³ Prior to data acquisition, K-wires with a diameter of 2.5 mm and a length of 150 mm (DePuy Synthes, USA), along with custom-made 3D-printed marker mounts equipped with infrared-sensitive fiducial markers, were mounted to each specimen. The K-wires were used to stabilize the bones of interest, including the lower leg and foot, to prevent bone movement during scanning. Optical markers were tracked by an optical tracking system (FusionTrack 500, Atracsys, Switzerland). A CT scan was performed on each specimen with an image resolution of 512×512 pixels, an in-plane resolution of 0.839 mm × 0.839 mm, and a slice thickness of 0.6 mm (NAEOTOM Alpha, Siemens, Germany). Bone segmentation was generated using the region growing and thresholding functionalities in Mimics (Materialise, Leuven, Belgium). For data acquisition, each specimen was scanned nine times using a tracked ultrasound device (AixplorerUltimate, SuperSonic Imagine, France) equipped with a linear probe that has an imaging frequency range of 4.0 to 15.0 MHz. The scanning procedure consisted of three forward and backward passes along the longitudinal axis of the tibia, three along the fibula, and three covering the foot (including the bones of the ankle joint such as the calcaneus and talus), aiming to maximize bone surface

²https://www.imfusion.com/

³Ethics approval has been granted by the Zurich cantonal ethics committee under BASEC Nr. 2023-01681.

coverage. Ultrasound images, along with the tracking data of the ultrasound probe and the specimen, were recorded with corresponding timestamps.

System Calibration. To determine the coordinates of the tracking fiducials on the specimen marker within the CT space, virtual spheres are created to match the size of the physical fiducials in MeshLab ⁴. These virtual spheres are initially manually aligned with the corresponding fiducials in the segmented CT model, followed by refinement using the point-to-point Iterative Closest Point algorithm [21]. The resulting registration transformation matrix allows for the accurate calculation of relative poses between the ultrasound probe and the bone CT model. However, converting each pixel of an ultrasound image into its corresponding point in the CT space requires accurate spatial calibration and accurate tracking of the ultrasound probe. In addition, temporal calibration is necessary to synchronize the ultrasound images with the tracking data. Following the convention in existing works [22, 23], we define the origin of the ultrasound image at the top-left corner. The pixels of the ultrasound image at timestamp t are defined in homogeneous coordinates as $\mathcal{P}^t = \left\{ \left[u, v, 0, 1 \right]^T \mid u \in [0, W), v \in [0, H) \right\}$, where W and H represent the image width and height, respectively. The corresponding point cloud in CT space, $\mathcal{U}^t = \left\{ \left[x_j, y_j, z_j, 1 \right]^T \mid j \in [0, H \times W) \right\}$, is computed as

$$\mathcal{U}^{t} = \mathsf{T}^{t+\Delta t}_{CT \leftarrow O} \cdot \mathsf{T}^{t+\Delta t}_{O \leftarrow US} \cdot \mathsf{T}_{US \leftarrow I} \cdot \mathsf{T}_{S} \cdot \mathcal{P}^{t} = \mathsf{T}^{t+\Delta t}_{CT \leftarrow US} \cdot \mathsf{T}_{US \leftarrow I} \cdot \mathsf{T}_{S} \cdot \mathcal{P}^{t} \tag{1}$$

where

$$\mathsf{T}_{US \leftarrow I} = \begin{bmatrix} r_{11} & r_{12} & r_{13} & d_x \\ r_{21} & r_{22} & r_{23} & d_y \\ r_{31} & r_{32} & r_{33} & d_z \\ 0 & 0 & 0 & 1 \end{bmatrix}, \quad \mathsf{T}_S = \begin{bmatrix} s_x & 0 & 0 & 0 \\ 0 & s_y & 0 & 0 \\ 0 & 0 & 1 & 0 \\ 0 & 0 & 0 & 1 \end{bmatrix}. \tag{2}$$

Here, T_S transforms 2D pixels into 3D points in the ultrasound image coordinate system, where s_x and s_y are the pixel dimensions in mm, as specified by the device. The transformation matrix $\mathsf{T}_{US\leftarrow I}\in \mathsf{SE}(3)$ (the Special Euclidean group in 3D) maps points from the image plane to the coordinate system of the ultrasound probe marker. Note that a transformation matrix $\mathsf{T}(\boldsymbol{\theta},\mathbf{d})$ can be defined using the Euler rotation angles $\boldsymbol{\theta}$ and the translation vector \mathbf{d} , which together specify the relationship between two coordinate systems. Similarly, $\mathsf{T}_{O\leftarrow US}^{t+\Delta t}\in \mathsf{SE}(3)$ and $\mathsf{T}_{CT\leftarrow O}^{t+\Delta t}\in \mathsf{SE}(3)$ represent transformations from the ultrasound marker to the optical tracking system and from the optical system to the CT space at timestamp $t+\Delta t$, respectively. The parameters of $\mathsf{T}_{O\leftarrow US}^{t+\Delta t}$ and $\mathsf{T}_{CT\leftarrow O}^{t+\Delta t}$ are provided by the optical tracking system. For simplicity, we denote $\mathsf{T}_{CT\leftarrow US}^{t+\Delta t}(\boldsymbol{\theta},\mathbf{d})=\mathsf{T}_{CT\leftarrow O}^{t+\Delta t}(\boldsymbol{\theta}_1,\mathbf{d}_1)\cdot\mathsf{T}_{O\leftarrow US}^{t+\Delta t}(\boldsymbol{\theta}_2,\mathbf{d}_2)$ as the direct transformation from the ultrasound marker to the CT space. The temporal offset Δt compensates for lag between tracking and ultrasound signals [22]. $\mathsf{T}_{US\leftarrow I}$ is determined via spatial calibration [23]. Unlike previous studies that treated spatial and temporal calibration independently [22, 23], we performed both calibrations simultaneously using a Z-phantom [23]. The temporal offset Δt was sampled over the range [-300,0) ms with a step size of 0.1 ms. For each Δt , $\mathsf{T}_{US\leftarrow I}$ was computed, and the corresponding

 $^{^4}$ https://www.meshlab.net/

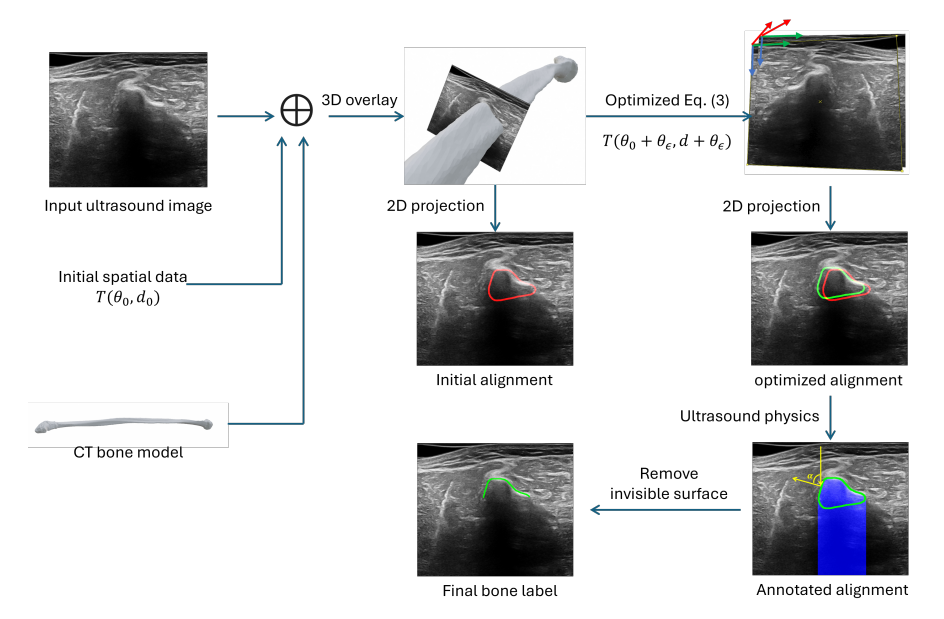


Fig. 2: Overview of the automated 2D bone labeling pipeline. By leveraging 3D spatial data, the ultrasound image and CT bone model are overlaid to produce an initial bone alignment (red). Optimization of Eq. (3) refines the alignment (green). Following the refinement, the bone shadow (blue) and incidence angles (yellow) are computed. Using ultrasound physics, invisible bone surface regions are excluded, resulting in the final bone label.

3D localization recorded. The optimal parameters were identified by minimizing the 3D localization error. Our method achieved a 3D localization error of 1.07 mm, outperforming previously reported errors (≈ 1.5 mm) [22, 23]. With precise calibration results, 2D pixel coordinates can be accurately mapped to 3D points in the CT space. For simplicity, we denote the pixel corresponding to the point $\mathbf{u}_i^t \in \mathcal{U}^t$ as $\mathbf{p}_i^t \in \mathcal{P}^t$, and define $f(\mathbf{u}_i^t)$ as the intensity value of \mathbf{p}_i^t in the original ultrasound image.

Bone Labeling. Points are sampled uniformly over the bone CT model to generate the CT point cloud \mathcal{C} . Both \mathcal{C} and \mathcal{U}^t (with original intensity values) are rendered in Figure 2. The CT-ultrasound bone surface intersection is defined as $\mathcal{I}^t = \mathcal{C} \cap \mathcal{U}^t = \{\mathbf{u} \in \mathcal{U}^t \mid \min_{\mathbf{c} \in \mathcal{C}} \|\mathbf{u} - \mathbf{c}\| \leq \gamma\}$ where γ is the parameter defining the thickness of the intersection ($\gamma = 0.3$ mm determined empirically). Ideally, \mathcal{I}^t can be projected back onto the ultrasound image, forming a complete bone label. However, as also reported previously [20], mismatches (1 to 2 mm) often occur due to accumulated errors, including tracking error, calibration error (see Figure 2). Although these mismatches are typically below 2 mm, they are noticeable given the high resolution of ultrasound images, which can reach up to 0.05 mm per pixel.

Bone contours that are roughly perpendicular to the ultrasound probe typically appear as high-intensity regions in ultrasound images due to the underlying ultrasound physics. Based on this principle, we propose an intensity-based optimization method

designed to refine the location of CT-derived labels. The proposed optimization relies on the following assumptions: (i) the main error sources are tracking and calibration errors, as the only undetermined variables in Eq. (1) are the tracking matrices $(\mathsf{T}_{CT\leftarrow O}^{t+\Delta t}$ and $\mathsf{T}_{O\leftarrow US}^{t+\Delta t})$ and the calibration matrix $(\mathsf{T}_{US\leftarrow I})$; (ii) pixels with high intensity in the vicinity of the non-corrected labels mostly correspond to the true bone contour. Beneath the bone shadow, there are almost uniformly dark regions, as bones possess the highest acoustic impedance compared to the surrounding soft tissues, causing most acoustic waves to be reflected back; (iii) the CT-ultrasound alignment error does not exceed an mean distance of 2 mm, given that the optical tracking system offers submillimeter accuracy⁵ and the calibration matrix achieves a 3D localization error of 1.07 mm. Furthermore, a random image sampled from each ultrasound sweep to measure mismatch yielded a mean error of 1.13 \pm 0.606 mm.

The key principle of our optimization method is to add small perturbations $(\boldsymbol{\theta}_{\epsilon})$ and \mathbf{d}_{ϵ} to the ultrasound image poses in order to maximize the intensity of pixels at the intersection between the ultrasound image and bone CT model while minimizing deviations from the recorded tracking data. We define the perturbed point cloud as $\mathcal{U}^{t}(\boldsymbol{\theta}_{\epsilon}, \mathbf{d}_{\epsilon}) = \mathsf{T}^{t+\Delta t}_{CT\leftarrow US}(\boldsymbol{\theta}+\boldsymbol{\theta}_{\epsilon}, \mathbf{d}+\mathbf{d}_{\epsilon}) \cdot \mathsf{T}_{US\leftarrow I} \cdot \mathsf{T}_{S} \cdot \mathcal{P}^{t}$ and the perturbed intersection as $\mathcal{I}^{t}(\boldsymbol{\theta}_{\epsilon}, \mathbf{d}_{\epsilon}) = \mathcal{C} \cap \mathcal{U}^{t}(\boldsymbol{\theta}_{\epsilon}, \mathbf{d}_{\epsilon})$. The proposed solution is written as:

$$\underset{\boldsymbol{\theta}_{\epsilon}, \mathbf{d}_{\epsilon} \in [-1, 1]^{3}}{\operatorname{arg\,max}} \frac{\sum_{\mathbf{u} \in \mathcal{I}^{t}(\boldsymbol{\theta}_{\epsilon}, \mathbf{d}_{\epsilon})} f(\mathbf{u})}{|\mathcal{I}^{t}(\boldsymbol{\theta}_{\epsilon}, \mathbf{d}_{\epsilon})|} - \lambda \frac{\sum_{i} ||\mathsf{T}(\boldsymbol{\theta}, \mathbf{d}) \cdot \mathbf{F}_{i} - \mathsf{T}(\boldsymbol{\theta} + \boldsymbol{\theta}_{\epsilon}, \mathbf{d} + \mathbf{d}_{\epsilon}) \cdot \mathbf{F}_{i}||_{2}}{N}$$
(3)

 \mathbf{F}_i denotes the homogeneous coordinate vector of the *i*-th tracking fiducial of the ultrasound probe marker, with N fiducials in total. The first term of equation (3) represents the mean intensity values of points in $\mathcal{I}^t(\boldsymbol{\theta}_{\epsilon}, \mathbf{d}_{\epsilon})$ under the corrected image pose. The second term represents the mean deviation of the tracking fiducials induced by the pose correction in terms of Euclidean distance. By leveraging the bounded set and regularization term, our approach ensures the solution remains close to the initial tracking data. The weighting parameter λ is empirically determined from the range [0.01, 0.1, 1, 10, 100,1000]. The optimization problem is solved using the differential evolution method [24]. Each λ value was tested on randomly sampled frames, and the results were evaluated quantitatively to select the optimal λ . To identify failed optimizations, a validation step is performed. Specifically, ultrasound images with a mean fiducial location correction greater than 1 mm after optimization are discarded. as the tracking device provides sub-millimetric accuracy. After the validation step, approximately 18.7% frames are discarded, with the mean fiducial location correction of the remaining frames being 0.481 mm. An example of a full bone label refined using the proposed optimization is shown in Figure 2.

To account the bone shadow effect, bone regions within the shadow (blue region in Figure 2) are discarded. In addition, we project the normal vectors from the bone CT model onto the ultrasound images and compute the incidence angles α between the projected normal vectors and the vertical scan lines, as shown in Figure 2. According to ultrasound imaging physics, the intensity of bone pixels decreases as α increases, with $\alpha > 90^{\circ}$ being a critical boundary. In this study, we keep bone pixels with $\alpha \leq 85^{\circ}$

⁵https://atracsys.com/fusiontrack-500/

to avoid boundary cases. An example of final bone label is shown in Figure 2. More examples are provided in the supplementary material.

To clinically evaluate the quality of bone annotations following our optimization pipeline, an expert physician specialized on orthopedic sonography assessed the quality of both the initial and optimized bone annotations. For comparison with state-of-the-art, we also employed the traditional "ultrasound to CT registration" algorithm available in the ImFusion Suite⁶ (ImFusion, Munich, Germany) to compute a global transformation matrix for registering the ultrasound data to the CT volume. In our experiment, one frame was randomly sampled from each ultrasound sweep, resulting in a total of 119 frames. Bone annotations were performed using three alignment methods: the initial alignment, the optimized alignment derived from our method, and the bone alignment obtained after the CT-US registration step. The resulting bone alignment outputs from these three methods were presented to an expert physician specialized on orthopedic sonography in random order. The expert evaluated the quality of each bone alignment using the following criteria:

- 0: Poor alignment, with large sections showing visible errors exceeding 3 mm.
- 1: Moderate alignment, characterized by some sections with visible errors between 1–3 mm
- 2: Good alignment, exhibiting only minor visible errors below 1 mm.
- 3: Excellent alignment, with no visible errors.

3.2 Bone Segmentation

Segmentation Mode. A U-net with ResNet encoders is trained on UltraBones100k to automatically segment bones in ultrasound images. The segmentation loss function being used is a combination of Dice Loss and Binary Cross Entropy Loss (implementation details are provided in the supplementary material). We split the dataset into 10 training specimens, 1 validation specimen, and 3 test specimens (around 25k ultrasound images). The training and validation sets are further split using cross-validation. For the test set, 700 randomly sampled ultrasound images were manually labeled by an expert surgeon, who identified the hyperechoic bone surface layer and its accompanying acoustic shadow using anatomical knowledge and real-time feedback. (detailed in the supplementary material)

Evaluation Metrics. In previous studies [14, 15], over 18 metrics were used for evaluating bone segmentation in ultrasound images, including intersection-based (e.g., Dice score) and distance-based metrics (e.g., one-sided CD), which complicates fair benchmarking of models. Bone labels in ultrasound are thin, even small shifts can drastically reduce intersection-based scores. While CD is easy to interpret, it struggles with false positives. To address this, we propose using distance-thresholded accuracy, completeness, and F1-score, which balance intersection-based and distance-based evaluations. Accuracy represents the fraction of correct predictions out of all predictions at a certain distance threshold, while completeness measures the fraction of correct predictions relative to the ground truth. Explicit formulations of these metrics are provided in the supplementary material. Particularly, our evaluation is based

⁶https://www.imfusion.com/

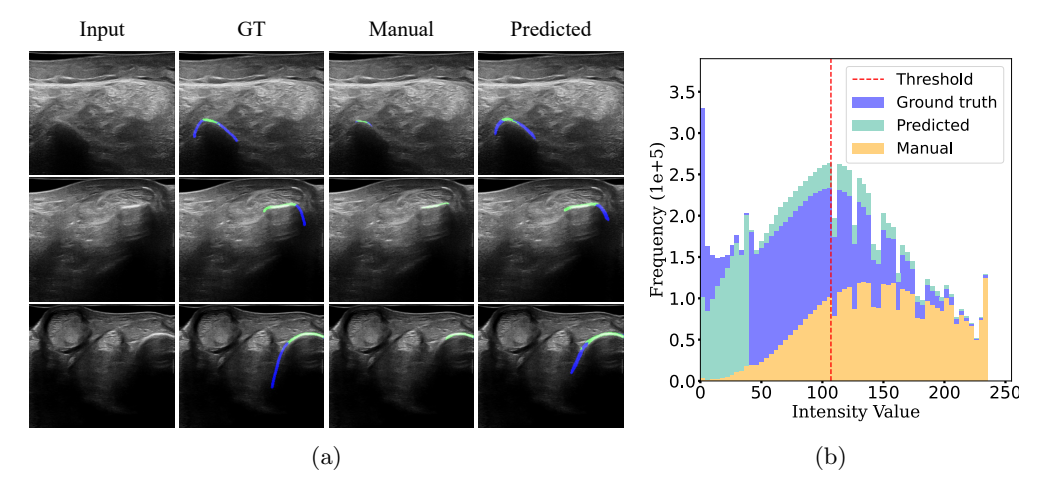


Fig. 3: (a) Qualitative comparison between manual labels and predicted ones. The first column shows the input images, the second column shows the CT-derived ground truth labels, the third column shows the manual labels, and the last column shows the bone labels predicted by the model trained on our labels. The bone labels are divided into high-intensity regions (green) and low-intensity regions (blue). (b) Distribution of pixel intensities over labels for manually labeled images. The red line represents the threshold determined by the Otsu method. While manual labels are mostly located in high-intensity regions, the proposed CT-derived labels allows for predictions in both high-intensity and low-intensity regions.

on the CT-derived labels, allowing to compare the performance between automatic segmentation and manual labeling.

To particularly assess the performance of our method in segmenting lower-intensity bone regions, we quantitatively divide the labels into high-intensity and low-intensity regions. The intensity values of all bone pixels in the collected ultrasound images are recorded, and the Otsu method is applied to determine an intensity threshold separating the bone pixels into two classes: high-intensity and low-intensity. The threshold is chosen to minimize intraclass variance and maximize interclass variance. Exemplar results are shown in Figure 3.

4 Results and Discussion

With our methodology, we have collected a dataset of 100k annotated ultrasound images with bone labels from 14 human cadaveric lower legs. The specimens have different physical characteristics, with heights ranging from 155 to 185 cm, weights from 59 to 99 kg, and BMI values between 19 and 30. The age range spans from 41 to 76 years, and the dataset includes both male and female specimens. Furthermore, arthritis status is documented, with some specimens having a history of falls or related conditions.

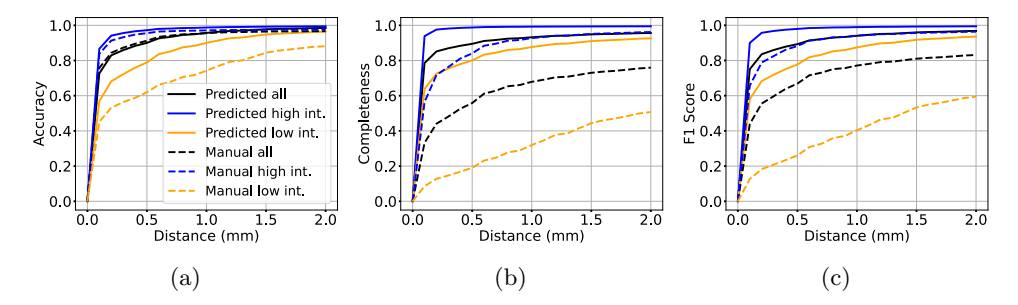


Fig. 4: Quantitative comparison between manual and predicted bone labels.

For the bone annotation rating experiment, the mean ratings are 1.45 for the initial alignment, 0.87 for CT-US registration, and 2.39 for our optimized alignment (box plot available in the supplementary material). A Wilcoxon signed-rank test with Bonferroni correction demonstrated a significant improvement in bone labeling quality following our optimization pipeline (p < 0.001). Unlike the traditional CT-US registration method, which calculates a single global transformation matrix for the entire ultrasound sweep to maximize overlapping voxel intensities, our approach computes a transformation matrix for each individual ultrasound frame. By leveraging the initial bone alignment as a prior, our method achieves significantly improved bone annotations.

Qualitative results between the manual bone labels and the model-predicted labels are shown in Figure 3 (additional results are provided in the supplementary material). The results indicate that the model trained on UltraBones100k outperforms the surgeon in segmenting bones in ultrasound images. Manual labels mostly include only high-intensity bone regions. In contrast, predicted bone labels include both high-intensity and low-intensity regions.

Quantitative results, including accuracy, completeness, and F1 score, are presented in Figure 4, demonstrating that the trained model consistently outperforms surgeon's manual labeling, regardless of the distance threshold used. On average, at a distance threshold of 0.5 mm, the trained model achieves an accuracy of 0.900, completeness of 0.895, and an F1 score of 0.893 across all bone regions. Particularly, for low-intensity regions, the accuracy of the trained model (0.789) is 27.4% higher than that of manual labeling (0.619), the completeness (0.801) is 320% higher compared to manual labeling (0.190), and the F1 score (0.778) is 197% higher than the manual labeling (0.261). These results in combination with the intensity distribution of labels illustrated in Figure 3b confirm that the expert surgeon faces difficulty in correctly labeling bone contours in low-intensity regions. These findings underscore the superiority of our approach over the manual labeling.

Previous work [20] aimed to align a tracked CT bone model with tracked ultrasound images. However, it was found that a mismatch of 1–2 mm was too large to allow for accurate automatic bone labeling in ultrasound images, necessitating manual bone labeling. In contrast, our optimization pipeline enhances CT-ultrasound alignment, facilitating automatic accurate bone label generation.

Generalizability The advantage of our method is that CT images are required only during pretraining. As demonstrated, this pretraining can even be conducted on ex-vivo anatomy, ensuring that no patients are exposed to ionizing radiation with our approach. Therefore it will not affect the current clinical workflow. Examples of ultrasound images depicting the pelvis and femur from a new specimen, along with the corresponding predicted bone labels by the model pretrained on UltraBones100k, are presented in the supplementary material, which demonstrate the generalizability of the pretrained model. The generalizability arises from the relatively consistent appearance of bones in ultrasound images. Bones, surrounded by soft tissues, exhibit highest acoustic impedance, appearing as bright curves or lines. Unlike other imaging methods, 2D ultrasound captures only partial bone segments, often unaffected by overall anatomical shape. Shared structural features across bones, such as in the arms and legs, further enhance model generalization. However, depending on the required level of accuracy, additional data collection may be necessary for specific anatomies and pathologies. In some cases, this may include collecting of in-vivo data. Conducting data collection studies with a limited number of patients is a common and justifiable approach in such scenarios.

5 Conclusion

Our methodology presents a promising solution to create large-scale and highly accurate training data without relying on expert labeling. Serving as a first benchmark, the segmentation model trained on UltraBones100k outperformed an expert surgeon with significantly more complete bone labels, demonstrating its potential for downstream tasks and clinical application. Further validation is needed to assess the application to other anatomies and ultrasound devices, which will be addressed in future work.

Acknowledgement

This research has been funded by the Innosuisse Flagship project PROFICIENCY No. PFFS-21-19. This work has also been supported by the OR-X, a Swiss national research infrastructure for translational surgery, and associated funding by the University of Zurich and University Hospital Balgrist.

References

- [1] Blankstein, A.: Ultrasound in the diagnosis of clinical orthopedics: The orthopedic stethoscope. World J Orthop 2: 13–24 (2011)
- [2] Khoury, V., Cardinal, E., Bureau, N.J.: Musculoskeletal sonography: a dynamic tool for usual and unusual disorders. American Journal of Roentgenology 188(1), 63–73 (2007)
- [3] Garcia, T., Hornof, W.J., Insana, M.F.: On the ultrasonic properties of tendon. Ultrasound in medicine & biology **29**(12), 1787–1797 (2003)

- [4] Hacihaliloglu, I.: 3d ultrasound for orthopedic interventions. Intelligent Orthopaedics: Artificial Intelligence and Smart Image-guided Technology for Orthopaedics, 113–129 (2018)
- [5] Ciganovic, M., Ozdemir, F., Pean, F., Fuernstahl, P., Tanner, C., Goksel, O.: Registration of 3d freehand ultrasound to a bone model for orthopedic procedures of the forearm. International journal of computer assisted radiology and surgery 13, 827–836 (2018)
- [6] Hacihaliloglu, I., Guy, P., Hodgson, A.J., Abugharbieh, R.: Automatic extraction of bone surfaces from 3d ultrasound images in orthopaedic trauma cases. International journal of computer assisted radiology and surgery 10, 1279–1287 (2015)
- [7] Li, R., Davoodi, A., Cai, Y., Niu, K., Borghesan, G., Cavalcanti, N., Massalimova, A., Carrillo, F., Laux, C.J., Farshad, M., Fürnstahl, P., Poorten, E.V.: Robot-assisted ultrasound reconstruction for spine surgery: from bench-top to pre-clinical study. International Journal of Computer Assisted Radiology and Surgery 18(9), 1613–1623 (2023)
- [8] Salehi, M., Prevost, R., Moctezuma, J.-L., Navab, N., Wein, W.: Precise Ultrasound Bone Registration with Learning-Based Segmentation and Speed of Sound Calibration. Paper presented at Medical Image Computing and Computer-Assisted Intervention MICCAI (2017)
- [9] Pandey, P., Guy, P., Hodgson, A.J., Abugharbieh, R.: Fast and automatic bone segmentation and registration of 3d ultrasound to ct for the full pelvic anatomy: a comparative study. International Journal of Computer Assisted Radiology and Surgery 13(10), 1515–1524 (2018)
- [10] Quader, N., Hodgson, A.J., Mulpuri, K., Schaeffer, E., Abugharbieh, R.: Automatic evaluation of scan adequacy and dysplasia metrics in 2-d ultrasound images of the neonatal hip. Ultrasound in Medicine & Biology 43(6), 1252–1262 (2017)
- [11] Baka, N., Leenstra, S., Walsum, T.: Ultrasound aided vertebral level localization for lumbar surgery. IEEE Transactions on Medical Imaging **36**(10), 2138–2147 (2017)
- [12] Villa, M., Dardenne, G., Nasan, M., Letissier, H., Hamitouche, C., Stindel, E.: Fcn-based approach for the automatic segmentation of bone surfaces in ultrasound images. International Journal of Computer Assisted Radiology and Surgery 13(11), 1707–1716 (2018)
- [13] Alsinan, A.Z., Patel, V.M., Hacihaliloglu, I.: Automatic segmentation of bone surfaces from ultrasound using a filter-layer-guided cnn. International Journal of Computer Assisted Radiology and Surgery 14(5), 775–783 (2019)

- [14] Pandey, P.U., Quader, N., Guy, P., Garbi, R., Hodgson, A.J.: Ultrasound bone segmentation: A scoping review of techniques and validation practices. Ultrasound in medicine & biology (2020)
- [15] Hohlmann, B., Broessner, P., Radermacher, K.: Ultrasound-based 3d bone modelling in computer assisted orthopedic surgery a review and future challenges. Computer assisted surgery (Abingdon, England) 29, 2276055 (2024)
- [16] Hohlmann, B., Broessner, P., Phlippen, L., Rohde, T., Radermacher, K.: Knee bone models from ultrasound. IEEE Transactions on Ultrasonics, Ferroelectrics, and Frequency Control 70(9), 1054–1063 (2023)
- [17] Gebhardt, C., Göttling, L., Buchberger, L., Ziegler, C., Endres, F., Wuermeling, Q., Holzapfel, B.M., Wein, W., Wagner, F., Zettinig, O.: Femur reconstruction in 3d ultrasound for orthopedic surgery planning. International Journal of Computer Assisted Radiology and Surgery 18(6), 1001–1008 (2023)
- [18] Liebmann, F., Stütz, D., Suter, D., Jecklin, S., Snedeker, J.G., Farshad, M., Fürnstahl, P., Esfandiari, H.: Spinedepth: A multi-modal data collection approach for automatic labelling and intraoperative spinal shape reconstruction based on rgb-d data. Journal of Imaging 7(9), 164 (2021)
- [19] Hein, J., Cavalcanti, N., Suter, D., Zingg, L., Carrillo, F., Calvet, L., Farshad, M., Pollefeys, M., Navab, N., Fürnstahl, P.: Next-generation surgical navigation: Marker-less multi-view 6dof pose estimation of surgical instruments (2023)
- [20] Zee, J.M., Fitski, M., Sande, M.A.J., Buser, M.A.D., Hiep, M.A.J., Scheltinga, C.E.J., Hulsker, C.C.C., Bosch, C.H., Ven, C.P., Heijden, L., Bökkerink, G.M.J., Wijnen, M.H.W.A., Siepel, F.J., Steeg, A.F.W.: Tracked ultrasound registration for intraoperative navigation during pediatric bone tumor resections with soft tissue components: a porcine cadaver study. International Journal of Computer Assisted Radiology and Surgery 19(2), 297–302 (2023)
- [21] Besl, P.J., McKay, N.D.: Method for registration of 3-d shapes. In: Sensor Fusion IV: Control Paradigms and Data Structures, vol. 1611, pp. 586–606 (1992). Spie
- [22] Mozaffari, M.H., Lee, W.-S.: Freehand 3-d ultrasound imaging: A systematic review. Ultrasound in Medicine & Biology 43(10), 2099–2124 (2017)
- [23] Li, R., Cai, Y., Niu, K., Poorten, E.V.: Comparative quantitative analysis of robotic ultrasound image calibration methods. In: 2021 20th International Conference on Advanced Robotics (ICAR), pp. 511–516 (2021)
- [24] Storn, R., Price, K.: Differential evolution a simple and efficient heuristic for global optimization over continuous spaces. Journal of Global Optimization 11(4), 341–359 (1997)

UltraBones100k: An Ultrasound Image Dataset with CT-Derived Labels for Lower Extremity Long Bone Surface Segmentation

Supplementary Material

This supplementary material provides technicalities and detailed analysis of the experiments that were omitted in the main paper due to space limitations. We provide the reader additional implementation details in Section 1. Then we share explicit formulations of the evaluation metrics in Section 2. In Section 4, we present additional quantitative and qualitative results.

1 Implementation details

The U-Net based model in Section 3.2 was implemented using the Segmentation Models Pytorch library 1 , with a ResNet152 encoder pretrained on ImageNet. The loss function is a weighted combination of Dice Loss (weight=1) and Binary Cross Entropy Loss (weight=1). We trained the model using the Adam optimizer with $\beta = (0.9, 0.999)$, starting with an initial learning rate of 1e-5, which decayed by 0.9 every 10 epochs. The training process ran for 100 epochs on an NVIDIA V100 GPU, with a batch size of 32. The code and pretrained model will be publicly available.

2 Evaluation Metrics

2.1 Bone Segmentation

Quantitative evaluations were carried out using distance-thresholded accuracy, completeness and F1 score between the predicted bone segmentation \mathcal{P} and ground truth \mathcal{G} . For a pixel $\hat{\mathbf{x}} \in \mathcal{P}$, its distance to the ground truth is defined as follows:

$$d_{\hat{\mathbf{x}} \to \mathcal{G}} = \min_{\mathbf{x} \in \mathcal{G}} ||\hat{\mathbf{x}} - \mathbf{x}||, \tag{1}$$

The accuracy, completeness, and F1 score are defined as follows:

$$Acc(\epsilon) = \frac{1}{|\mathcal{P}|} \sum_{\hat{\mathbf{x}} \in \mathcal{P}} [d_{\hat{\mathbf{x}} \to \mathcal{G}} < \epsilon]$$
 (2)

 $^{^{1}} https://github.com/qubvel-org/segmentation_models.pytorch \\$

$$Com(\epsilon) = \frac{1}{|\mathcal{G}|} \sum_{\mathbf{x} \in \mathcal{G}} [d_{\mathbf{x} \to \mathcal{P}} < \epsilon]$$
 (3)

$$F(\epsilon) = \frac{2Acc(\epsilon) \cdot Com(\epsilon)}{Acc(\epsilon) + Com(\epsilon)},\tag{4}$$

where [.] is the Iverson bracket and ϵ is the distance threshold. Accuracy represents the fraction of correct predictions out of all predictions, while completeness measures the fraction of correct predictions relative to the ground truth.

3 Manual Bone Annotation

The following description of manual bone annotation in ultrasound images is provided by the surgeon. "Bone surfaces in ultrasound images are identified as a hyperechoic (bright) layer resulting from the significant reflection of ultrasound waves at the bone-tissue interface. This bright layer is typically accompanied by a characteristic acoustic shadow extending posteriorly, as the underlying bone attenuates or reflects the majority of the ultrasound signal. The anatomical region being scanned significantly influences the clarity and confidence of bone surface identification. Larger bones (e.g., >1 cm in diameter) with smooth, superficial surfaces are more readily identified due to their distinct echogenicity and reduced interference from surrounding tissue artifacts or acoustic noise. In contrast, smaller or deeper bones, or those with irregular surfaces, may present more ambiguous features. Clinicians utilize their expertise in anatomy and sonographic imaging to accurately interpret these structures during live scanning. Experienced operators rely on a combination of real-time image feedback and their knowledge of anatomical landmarks to delineate tissue structures, including bone surfaces. This process underscores the operator-dependent nature of ultrasound-based diagnostics in clinical practice. For labeling purposes, the Labels software (ImFusion GmbH) was employed to annotate the bone surface layer on a pixel-wise basis within the acquired images. This software allows precise manual delineation of the bone surface, facilitating the creation of ground-truth labels for subsequent analysis."

4 Additional Results and Visualizations

Intensity-based optimization The effect of the intensity-based optimization (equation (1) in the main paper) applied on the CT-derived labels is shown in Figure 2.

Bone annotation rating experiment The results of the bone annotation rating experiments are presented in Figure 1.

Bone segmentation Additional comparisons between manual labels and contour predicted by a model trained using the proposed labels are shown in Figure 3. As can be seen, the model trained using the proposed CT-derived labels provides much more complete bone contours.

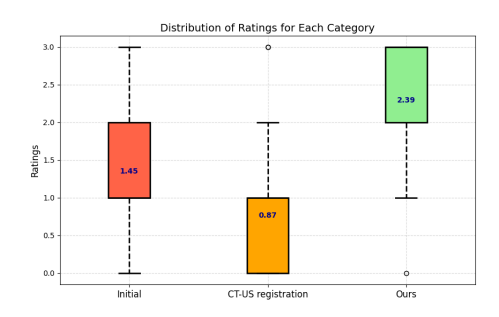


Figure 1: Results of the rating experiment.

Transferability Examples of ultrasound images depicting the pelvis and femur, along with the corresponding predicted bone labels, are presented in Figure 4.

Bone surface reconstruction To demonstrate the capability of our dataset for high-quality bone surface reconstruction, we applied state-of-the-art (SOTA) methods, including FUNSR [1], to our data. The outcomes of these applications are depicted in Figure 5 for the tibia and Figure 6 for the ankle, respectively.

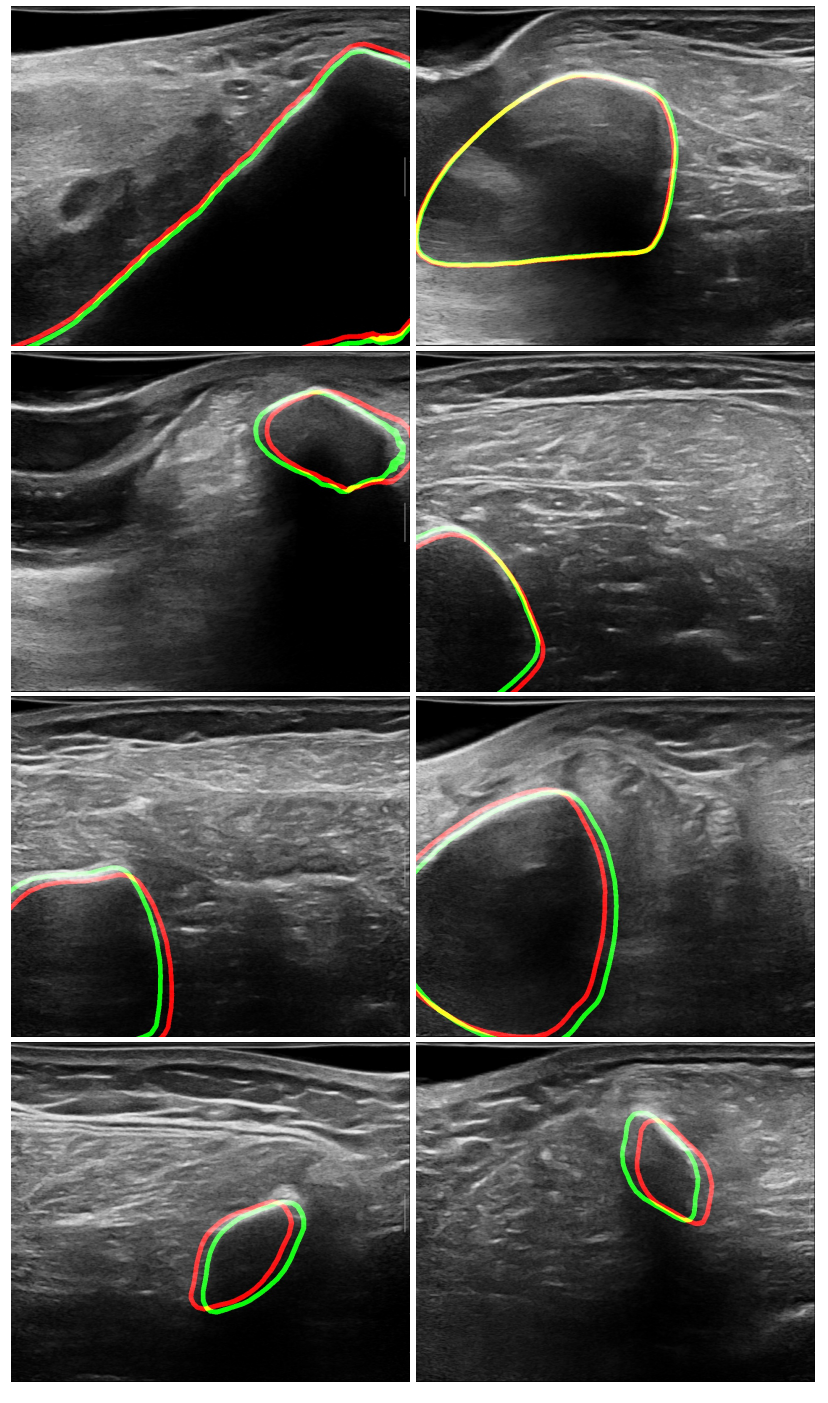


Figure 2: Comparison results of bone annotation before and after optimization. Red regions show the initial alignment, green regions show the refined alignment, yellow regions are the overlap.

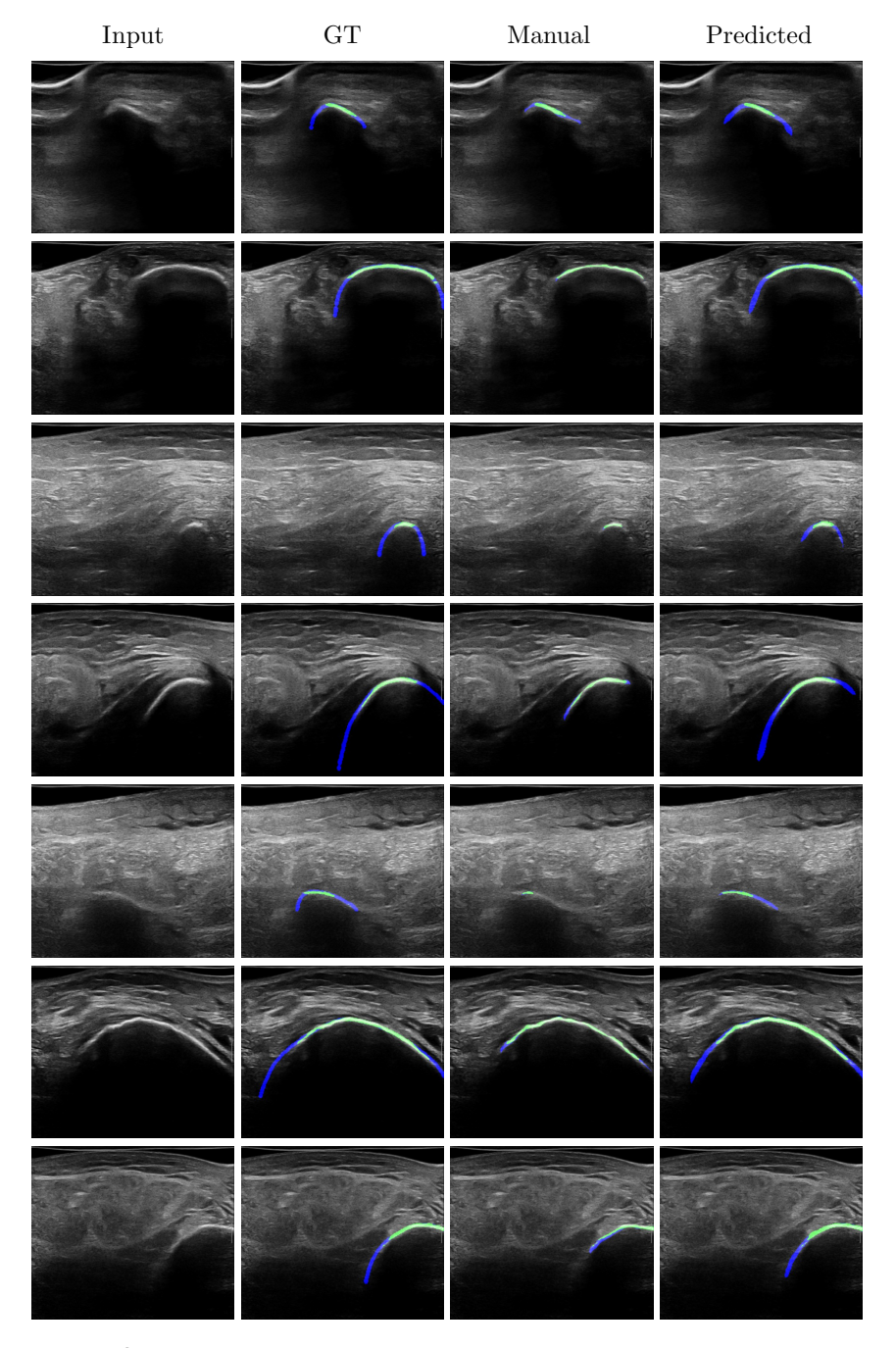


Figure 3: Qualitative comparison between manual annotations and trained bone annotations. The first column shows the input images, the second column shows the ground truth labels, the third column shows the manual annotations, and the last column shows the bone annotations predicted by the trained model. The bone annotations are divided into high-intensity regions (green) and low-intensity regions (blue).

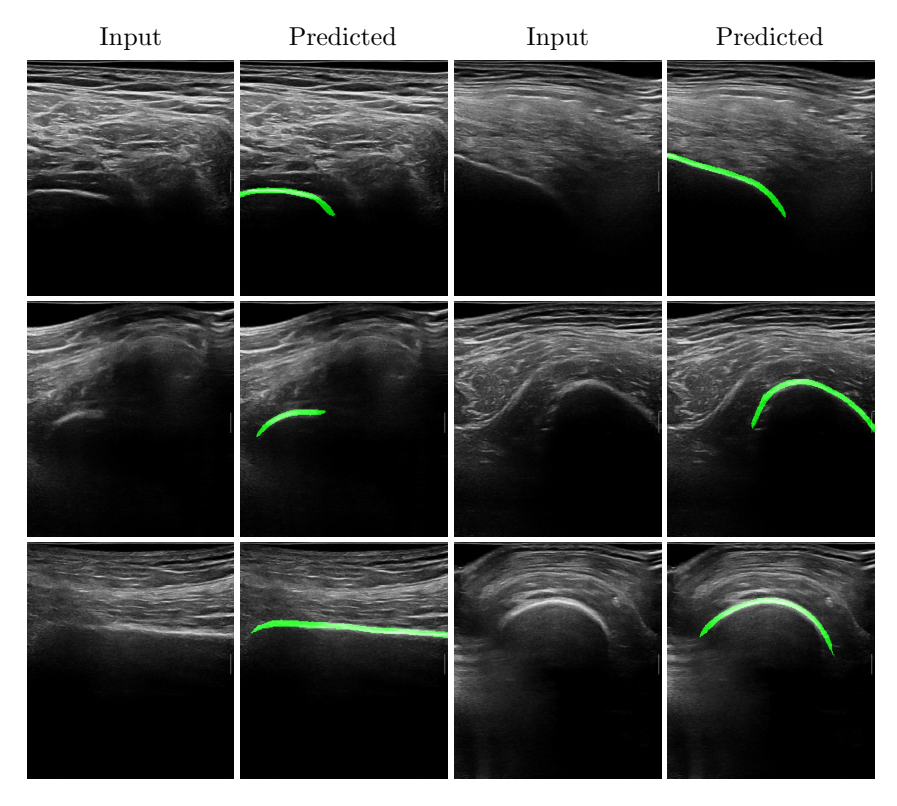


Figure 4: Examples of ultrasound images depicting the pelvis and femur, along with the corresponding predicted bone labels.

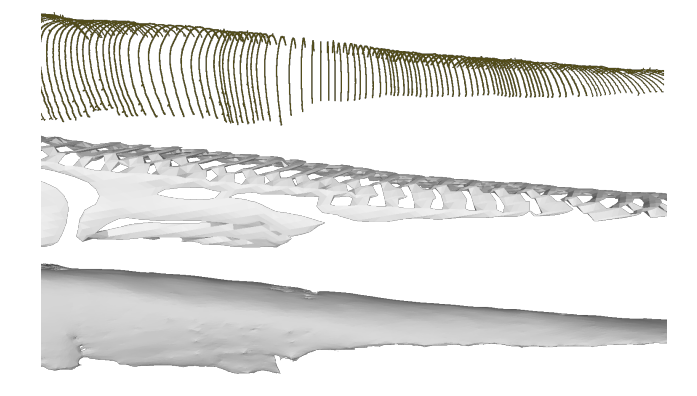


Figure 5: Bone surface reconstruction result for the tibia. The first row shows the tracked bone segmentations. The second row shows the result by FUNSR, with a one-sided Chamfer Distance of 0.828 mm and a 95% Hausdorff Distance of 1.920 mm. The third row shows the result by the traditional volume interpolation method, with a Chamfer Distance of 0.652 mm and a 95% Hausdorff Distance of 1.496 mm.

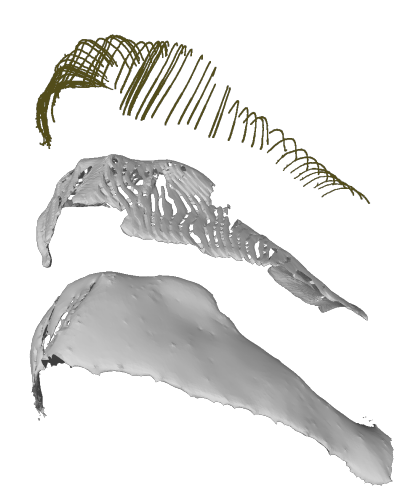


Figure 6: Bone surface reconstruction result for the calcaneous. The first row shows the tracked bone segmentations. The second row shows the result by FUNSR, with a one-sided Chamfer Distance of 0.731 mm and a 95% Hausdorff Distance of 1.811 mm. The third row shows the result by the traditional volume interpolation method, with a Chamfer Distance of 0.680 mm and a 95% Hausdorff Distance of 1.552 mm.

References

[1] H. Chen, L. Kumaralingam, S. Zhang, S. Song, F. Zhang, H. Zhang, T.-T. Pham, K. Punithakumar, E. H. Lou, Y. Zhang, L. H. Le, and R. Zheng. Neural implicit surface reconstruction of free-hand 3d ultrasound volume with geometric constraints. *Medical Image Analysis*, 98:103305, 2024. ISSN 1361-8415. URL https://www.sciencedirect.com/science/article/pii/S1361841524002305.